Correlation of a 410-km discontinuity low velocity layer with velocity tomograms along the RISTRA line array sampling across Utah, New Mexico and west Texas

2010 IRIS Workshop

Zhu Zhang and Ken Dueker
Department of Geology and Geophysics, University of Wyoming, Laramie, Wyoming 82071

ABSTRACT

The transition zone water-filter model (Bercovici and Karato, 2003) predicts that a hydrous melt flux is produced in upwelling region. This prediction is tested via stacking of P-wave receiver function using the combined IRIS-PASSCAL RISTRA 1.0 and 1.5 line arrays that cross west-Texas, New Mexico and Utah. A total of 1202 radial component receiver functions are calculated from 86 teleseismic P-wave data with M_b>5.5 at distances of 30°-95°. The receiver functions are generated by using extended-time multi-taper spectral estimation method with a Gaussian 0.2 Hz low-pass frequency. The receiver functions are binned into the NW, SE, SW earthquake azimuthal quadrants and stacked to produce well-resolved images of the 410 and 660 km discontinuities. The depths of the two primary discontinuities vary from 395-426 km for the '410' and from 649-678 km for the '660'. With respect to the vertical component, the average amplitudes of the discontinuities are 3.0% ('410') and 2.8% ('660'). Where observed, the 410 low velocity layer (410-LVL) arrival has a -1.8% amplitude which is over twice as large as the side-lobe of the positive amplitude '410' arrival. The three receiver function quadrant stacks finds a correlation between the occurrence of a 410-km low velocity layer and teleseismic body wave velocity tomogram (Schmandt and Humphreys, in review). The 410-LVL arrival is absent where the velocities about the 410 km discontinuity are high and the 410-LVl arrival is present where the velocities are low. Our finding is consistent with the transition zone water filter model which predicts the production of a hydrous melt layer only where upflow of sufficiently hydrated transition zone mantle occurs. Additional effects on the melt layer occurrence (and thickness) due to lateral porous flow of the slightly molten layer driven by '410' topography complicates the correlation of the 410-LVL with respect to the mantle flow direction inferred from the velocity tomograms. Also, the long-term melt layer thickness depends to first order on the sinks which Karato and Bercovici call viscous entrainment due to downflow across the 410 (Fig. 1).

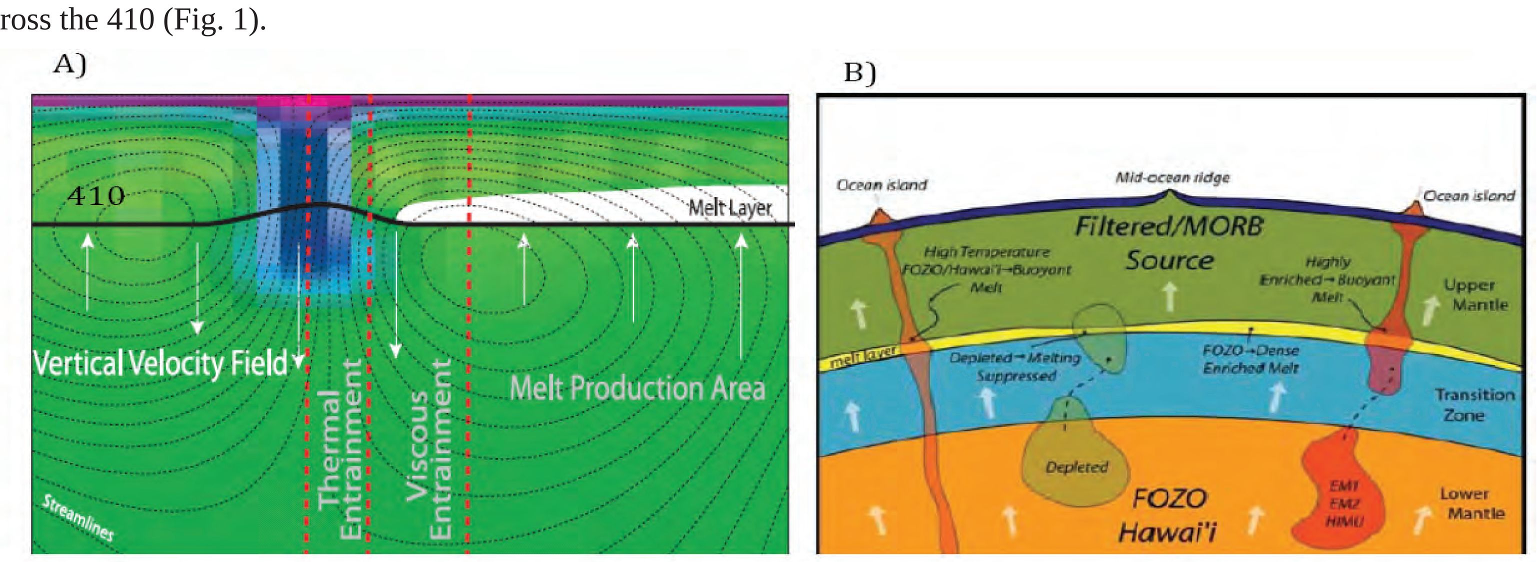

Figure 1. Transition zone water filter model (Karato et al., 2006). A) Melt layer production in the upwelling regions and melt layer viscous entrainment (melt layer destruction via quenching) in downwelling regions. The flow is driven by the slab down-flow (blue thermal anomaly) and the flow streamlines are shown as dashed lines. B) Plume of buoyant upwelling from 410-km discontinuity melt diapir labeled as an 'ocean island'.

INTRODUCTION

The seismic velocity discontinuities at 410-km and 660-km depth are due to phase change from olivine $(Mg,Fe)_2SiO_4$ to wadsleyite, and from ringwoodite to perovskite/magnesiowustite respectively. A 410-km low velocity layer (410-LVL) atop the 410 km discontinuity in seismic observations in many regions has been detected by P-wave triplication studies and P_{ds} receiver function analysis. The 410-LVL is interpreted as possibly dense hydrous partial-melt layers.

Bercovici and Karato [2003] proposed a hypothesis termed the transition-zone water-filter model, which predicts that ambient mantle filters off incompatible elements into the melt phase as it ascends from high-water-solubility transition zone into low-solubility upper mantle above the 410km discontinuity (Fig. 1).

Teleseismic body-wave tomograms find a high velocity anomaly in the transition zone beneath western Utah and northeastern Nevada (Fig. 2, 3; [Schmandt and Humphreys, in review; Sine et al., 2008]). Prior seismic P_{ds} analysis from the PASSCAL RISTRA 1.0 array has found a mean 32 km thick low velocity layer atop the 410 km discontinuity with a 5-6% shear wave velocity reduction [Jasbinsek et al., 2010].

Given the previous seismic observations of 410-LVL, we propose a hypothesis that low velocity anomalies above the 410-km discontinuity manifest the transient upward shedding of diapir from the 410-LVL.

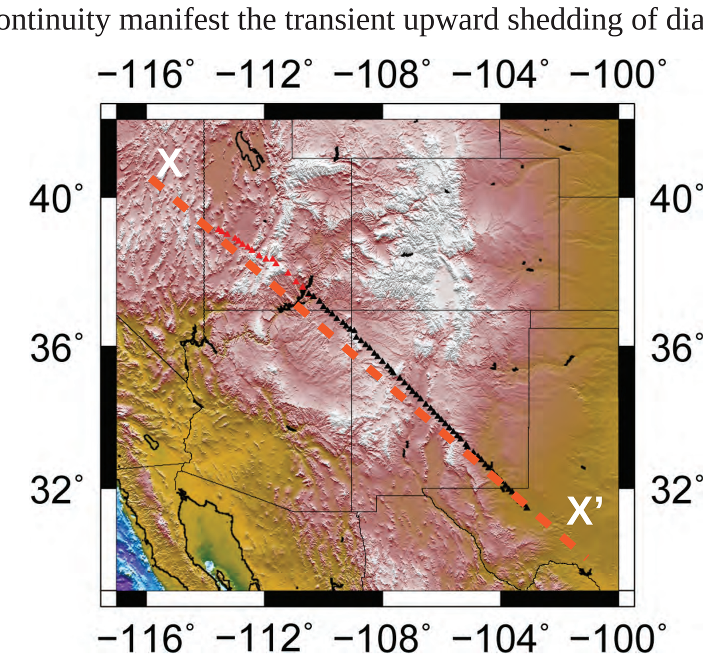

Figure 2. The topography with station locations of the RISTRA seismic array. Black triangles are stations of RISTRA1.0 and red triangles are stations of the RISTRA1.5. X-X' is cross section line.

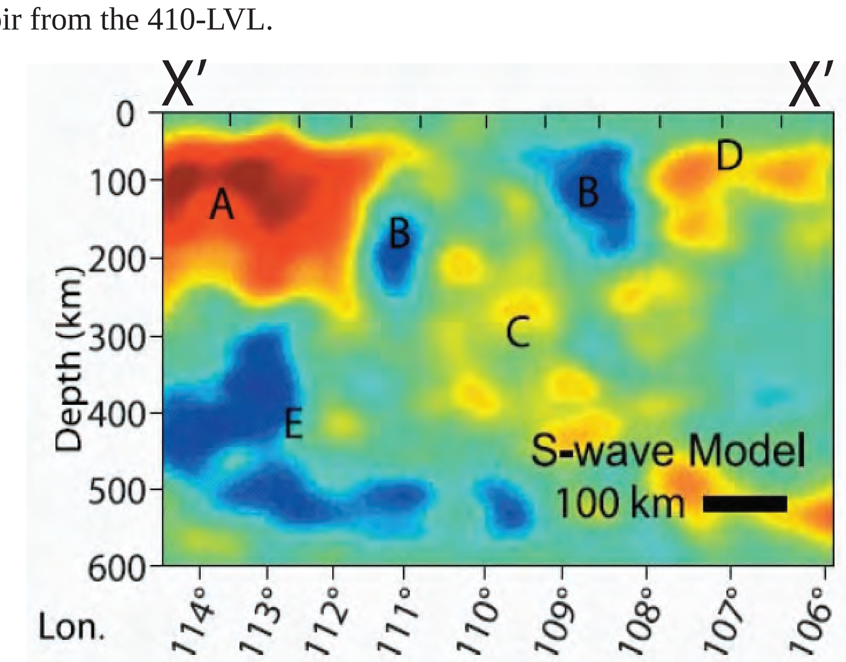

Figure 3. Teleseismic S wave tomography cross-section (X-X' in Fig. 2) from Sine et. al. (2008). Region A-E are velocity anomalies, and E is interpreted to be a sinking 24 Ma old segment of Farallon slab.

METHOD AND DATA

The combination of the RISTRA1.0 and 1.5 seismic arrays (Fig. 2) forms a 1400-km linear array of 72 broadband seismometers with ~20-km station spacing. 86 events with Mb > 5.5 and at 30° – 95° distances are collected for P-to-S receiver function analysis (Fig. 4). P-waveform spectra are estimated using the Extended-Time Multi-Taper estimation [Helffrich, 2006]. A low cut-off $\cos^2$ frequency-domain taper of 0.2 Hz is applied to the spectral estimation. After calculation, a 3-30 s filter is applied to the receiver functions. The radial components of receiver functions are mapped from time to depth based on average vertical velocity profile in study region from P wave model [Burdick, et al., 2008]. The S wave speed model is calculated by fixing Vp/Vs ratio to 1.76 for the crust and 1.82 for the mantle.

A total of 1965 radial receiver functions are calculated. The dataset of receiver functions is culled by RMS histogram culling, cross-correlation culling, and visual inspection. The culling results in 1202 radial receiver functions in the dataset. The retained radial receiver functions are binned and linearly stacked to create a set of NW, SE, SW quadrants stack traces with 9 overlapping bins with a width of 185-km and 50% bin overlap (Fig. 6).

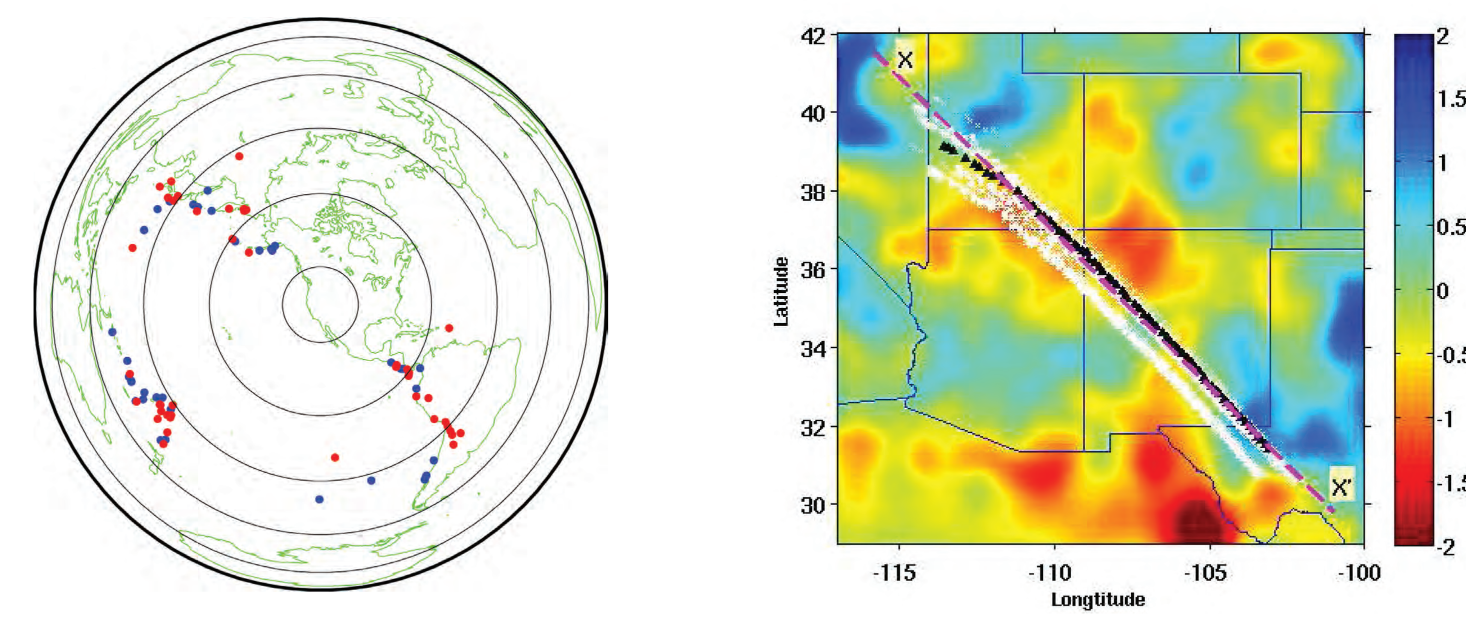

Figure 4. (Left) plot shows the events used in this study. Blue dots are events locations used by RISTRA 1.0 array, red dots are events locations for RISTRA 1.5. Circles are epicentral distances from center of the array with 15°, 45°, 75°, 105° and 135°. Right plot is P-wave speed tomography at the depth of 400-km overlaid with piecing points at the depth of 410-km [Schmandt and Humphreys, in review].

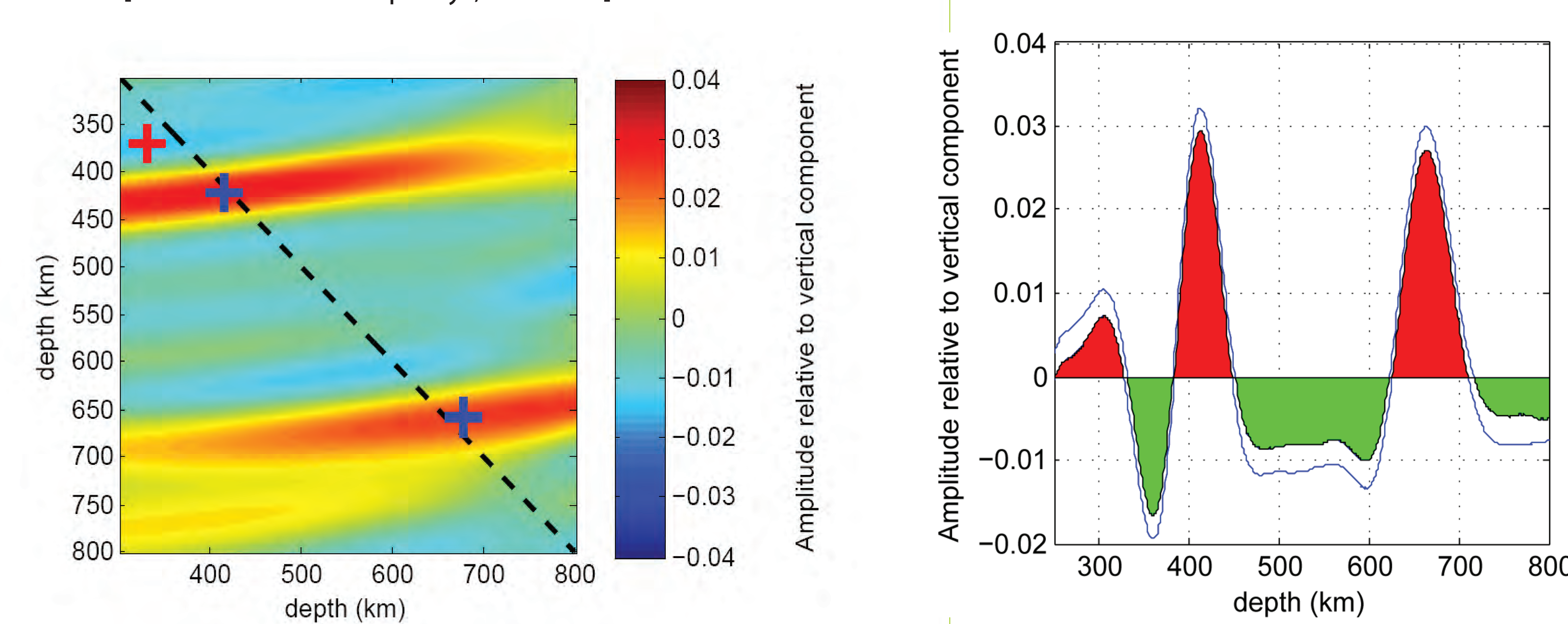

Figure 5. (Left) Phasing plot of global stacked radial receiver functions showing move out of 410-LVL (red cross), 410-km and 660-km discontinuities (blue crosses). The black dashed line is unity slope line which shows the line of predicted P_{ds} where the amplitude of P-S conversions should be maximal. (Right) Radial receiver functions stacking shows the 410-LVL, 410-km and 660-km discontinuities. Amplitude is normalized to Z component of the receiver functions. Error bar is standard deviation calculated using a bootstrap resampling algorithm.

CONCLUSION

We find that the velocities anomalies are correlated with the occurrence of 410-LVL. For the SE and SW quadrants, the amplitude of 410-LVL diminishes in bins at southeast end of the array. For NW quadrant, the 410-LVL diminishes at northwest end of the array. This findings support the hypothesis that the water filter model is not operative in downwelling high velocity region. This correlation between the amplitude of 410-LVL and Vp perturbation is shown in Figure 7. The high velocity regions without a 410-lvl arrival indicate the lack of a melt layer.

RESULT

A stack of all receiver functions shows two positive polarity arrivals at the depth of 413-km and 664-km, respectively (Fig. 6). The mean thickness of transition zone is 251±7-km, which is 8 km thicker than the 243-km global average [Gu and Dziewonski, 2002]. The 410-LVL negative polarity arrival has an amplitude of 1.8% with respect to the zero-lag P-wave arrival on the Z component, and amplitudes of 410-km and 660-km discontinuities are 3.0% and 2.8% of the Z component, respectively. Phasing analysis is used to identify the arrivals displaying correct P_{ds} moveout (Fig. 5). A 31-km range of topography on 410-km discontinuity is measured from 395-km to 426-km, and a 29-km range of topography on the 660-km discontinuity is measured from 649-km to 678-km (Fig. 6).

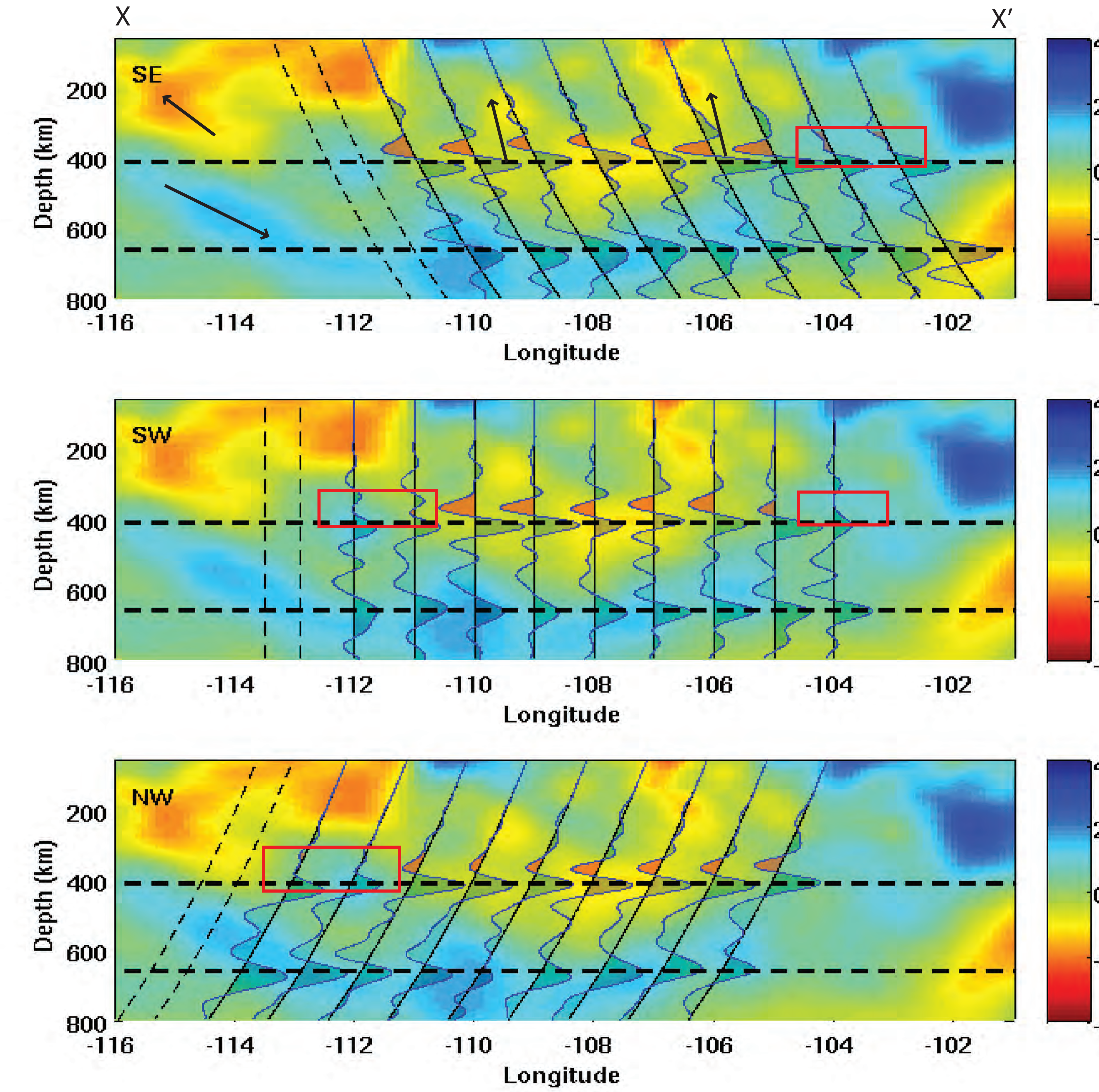

Figure 6. Three images of stacked radial receiver functions in nine 185-km wide bins from RISTRA array using SE (upper), SW (middle), and NW (lower) quadrants data are overlaid by P-wave speed tomograms cross-section from Schmandt and Humphrey [in review]. The two dashed lines on left side of images show scale of 3% amplitude variatoins relative to Z component receiver function. Positive amplitude arrivals are shaded black, and negative amplitude arrivals are shaded in light black, except the 410-LVL arrival which is shaded red. The amplitude of 410-LVL arrival is absent (boxed in red) or present where the velocities about the 410 km discontinuity are relatively high or low, respectively. The black arrows show the mantle flow directions.

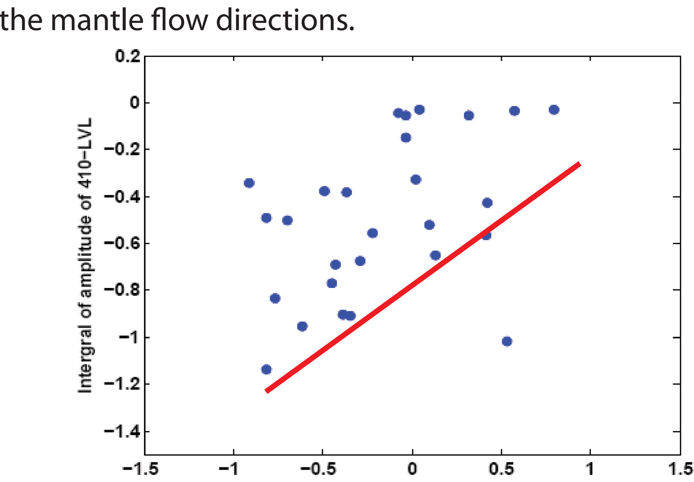

Figure 7. Scatter plot of integral amplitudes of 410-LVL versus Vp perturbation at the 410-km discontinuity. The red line shows a general trend with large 410-LVL arrival amplitudes with respect to reduced Vp velocities at the 410.